

Dynamics and Control of a Compliant In-Parallel-Actuated Mechanism

Lekan Molu

Abstract—A compliant multiple freedom parallel soft mechanism is here put forward to counterbalance mechanisms currently prevalent in precise collaborative robot manipulation tasks. We study the kinematics of the mechanism using continuum mechanics and elementary differential geometry. We then derive the Newton-Euler system of equations of its kinetics using elasticity theory. Relating the dynamic boundary value problem of the soft actuators' total Cauchy stress tensor to the force wrenches on the object/load, we write out the manipulation map and construct the associated Jacobian for its direct positioning analysis. We analyze the manipulability measure, manipulability ellipsoid, and grasp control for grasp configurations.

I. INTRODUCTION

In this paper, we will study a multi-degree of freedom robot composed of compliant and deformable shells as kinematic pairs; these pairs are constrained along the circumferential direction such that when pneumatically actuated, the pairs stretch symmetrically in a radial direction. The circumferential constraint reduces the soft actuators' freedoms; and the overall kinematic linkage preserves actuation freedoms that yield desired range of motions in six dimensions. The proposed mechanism is useful for the dexterous manipulation of an object in its workspace. We limit our scope to the constitutive mathematical model of the kinematic pairs' deformation; we discuss the system's number- and type-syntheses; and provide an analysis of the manipulability measure, manipulability ellipsoid, and kinematic and kinetic equations of motion and movement.

Rigid kinematic pairs [1], [2] within serial linkages and mechanisms [3] have played a major role in robotics and automation over the last few decades [4]. Inspired by the anthropomorphic human arm, these mechanisms possess inherent stiffness to prevent vibration and structural deformation as well as preserve positioning precision in well-structured manipulative tasks. Their low intrinsic freedoms [1] limit morphological computation [5]; moreover, their inherent lack of hyper-redundancy – being made up of one to three lower pairs [1] in most of their kinematic configurations – limit their suitability to articulated loads' manipulation, ambulation, or navigation tasks. In addition, they possess low load-to-mass ratios, so that transporting decent heavy loads in their workspace requires a lot of manipulator mass. Imposing forces and torques on the tool frame of the robot to solve a precise positioning problem typically introduces links' deformation and flexure, and internal sensors' drive backlash such that

† 3620 Hamilton Walk (John Morgan Building), University of Pennsylvania, Philadelphia, PA 19131, USA.
olalekan.ogunmolu@pennmedicine.upenn.edu

computed homogeneous transformations lack numerical precision to guarantee effective control. All of these make their use limited for unstructured manipulation tasks that require highly (nonlinear) dynamic dexterity such as juggling, composition of dynamic motions [6], head-and-neck manipulation in radiosurgery [7] and other dynamic human-robot collaborative tasks.

While there has been concerted efforts to design parallel manipulators that can transport heavier loads in recent years, most common parallel manipulators that have been proposed have a reduced workspace [8], often possess complex mechanical parts [9], non-trivial direct kinematics [10], multiple singular configurations [38], limited dexterity [2], not to mention the associated problems of mobility determination as more kinematic pairs, chains, members and loops are added to the mechanical system. Examples of common parallel manipulators are the six freedom Stewart platforms [11] – useful for precise positioning tasks where load weight distribution among links makes for effective and accurate manipulation, the Delta [12] and Tricept [9], [13] robots – which possess pick and place precision and machining effectiveness respectively.

Compliance in robot manipulators is a necessity for articulated manipulation of structures, in particular those with nonlinear and traditionally non-conformal geometry. Soft, compliant kinematic linkages and mechanisms exhibit distributed deformation in their configuration space [5], [14], [15] in addition to bending and twisting capabilities [16]. Their minimal resistance to applied strain and high load-to-weight ratio together with their distributed compliance make them choice mechanisms in collaborative human-robot automation domains.

When carefully designed, soft, compliant mechanisms can continuously deform their bodies and emulate biological motions, as well as adapt their geometry to an environment – employing embodied intelligence and morphological computation in order to manipulate objects [17]. These make them capable of more freedoms and hyper-redundancy in flexible articulated manipulation, ambulatory, locomotion, and navigation scenarios.

Contributions: While many soft mechanisms proposed to date typically conform to open kinematic chain design configurations [18], [18], [19], their mechanical architecture are not well-adapted to precision articulated automation tasks. Our goal here is to study a soft parallel architecture, guided by this pertinent question: how do we harness soft matter for useful human-collaborative robots (or cobots) in delicate workspaces– exploiting their intrinsic morphological computation properties – in order to yield simplified control laws for safety-critical manipulation? In emphasis and in scope, we

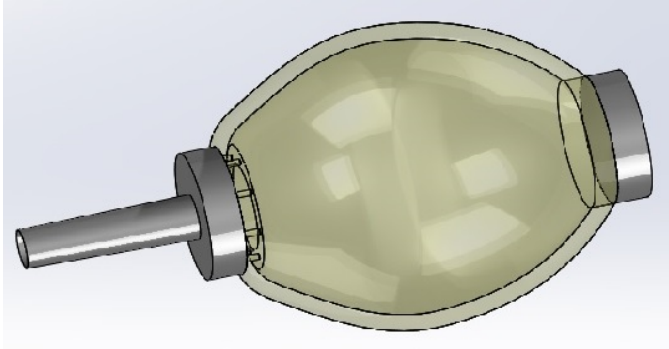


Fig. 1: Prototype of an IAB.

select a soft compliant mechanism, cast out of silicone material arranged around a human cranium region to accommodate. We develop a theoretical framework for the mechanism's kinetics and kinematics via a rigorous constitutive nonlinear elastic deformation synthesis and differential geometry, and analyze the control-based grasp of the articulated compliant mechanism for manipulation purposes.

Possible applications may be in the (i) animation industry where animated pluses need precise deformation to specific configurations [20], [21]; (ii) real-time control and simulation of hyperelastic materials [22], [23]; (iii) real-time closed-loop automatic motion deviation correction, particularly during beam-on time in robotic radiosurgery¹; or (iv) as a compatible soft robotic patient motion correction system in emerging frameless and maskless cranial manipulation in magnetic resonance imaging-linear accelerator radiation treatment of cancers [24], [25], where it can hasten the current treatment time in clinics, minimize patient discomfort post-treatment, or drastically improve dose efficacy so that the patient's treatment can be effectively fractionated [26].

The rest of this paper is organized as follows: in § II, we prescribe the mechanical model of the kinematic pairs and the system configuration. In § III, we describe the finite elastic deformation model and solve the dynamic boundary value problem. We then analyze the contact kinematics with the head in § IV and derive the dynamic equations in § V. In § VI, we derive the end-effector velocities and forces; and conclude the paper in § VIII. Proofs and derivations are provided in the appendices. The fabrication process for the mechanism described in section § II is described in § A

II. MECHANISM SETUP

We are concerned with inflatable air bladders (or IABs) [7] made out of elastomeric polymers, and possessing an internal air cavity that allows for compression or expansion of the elastomeric membrane structure along the circumferential and radial axes. Two plastic or rubber fitting connections can be connected to a low-pressure pneumatic air supply and vacuum respectively so as to facilitate air supply and removal for appropriate deformation. A simplified prototype is illustrated in Fig. 1. In general, when soft robots are assembled, the region where the assemblies are connected easily undergoes large

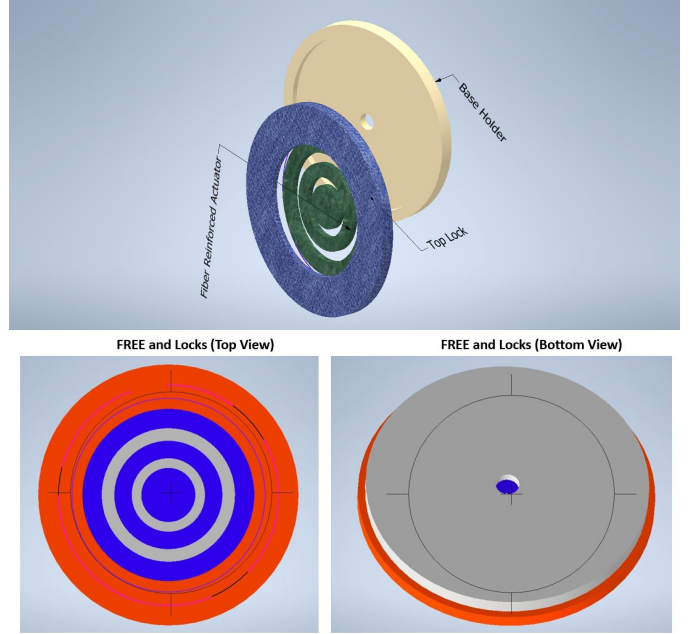


Fig. 2: CCOARSE FREEE assembly: Top: Components of the assembly. Bottom: Top(L) and bottom (R) views.

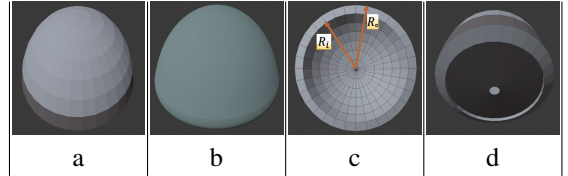


Fig. 3: (a) Patterned layers, (b) Gaussian curvature at full deformation, (c) Hollow chamber with radii, $\{R_i, R_o\}$, (d) Back.

stress, which can cause structural break-down. To overcome this, we have proposed a hybrid actuator module, combining the IAB structure in Fig. 1 and semi-rigid components, made of cut resistant polycarbonate acrylic materials. Because the modules push against each other through a rigid surface, the actuator possesses good force transmission while maintaining high elasticity when compressed by load forces or pneumatically expanded. In addition, to simplify the kinematic model of the elastomeric continuum during numerical computations, a fabric constraint has been added to the elastomeric membrane to constrain deformation along the circumferential axis. This is consistent with recent circumferentially-constrained and radially symmetric design such as proposed by authors [27]. The mechanism design template is given in Fig. 2. This sealing mechanism aids radiation transparency during radiation delivery to the head and neck region, an important requirement in robotic radiation therapy and stereotactic radiosurgery [28] where the immobilization mechanism must not attenuate dose radiation. Fig. 3 depicts the expected geometrical behavior of the IAB after deformation.

We position IABs around the patient's cranium as illustrated in Fig. 13. The IABs are held in place around the head by a low-temperature rigid PVC foam insulation sheet, encased in carbon fiber to prevent radiation beam attenuation. Velcro stickers (not shown) hold the IABs in place. The freedoms provided by each IAB within the setup in Fig. 13b are

¹The actual time that a radiation source is producing ionizing radiation.

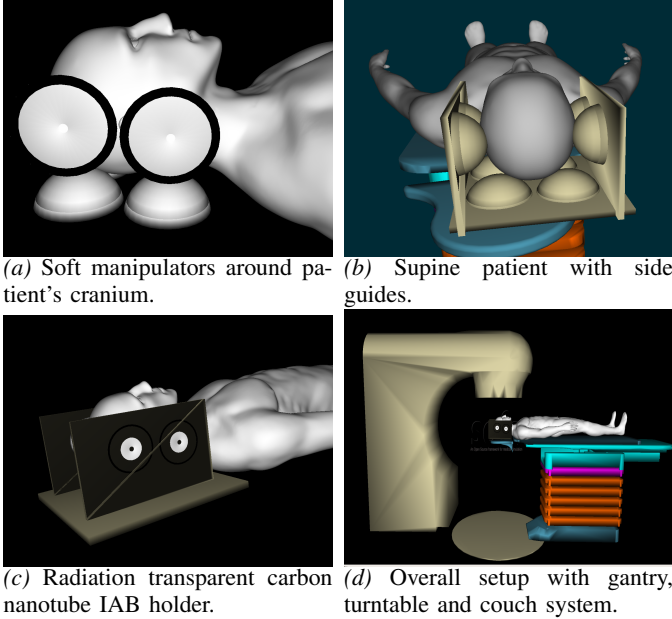


Fig. 4: System setup.

described as follows: the side actuators correct head motion along the *left-right* axis of the head anatomy, including the yaw and roll motions, while the base IABs correct the head motion along the *anterior-posterior* axis [1, Ch. 2]. This arrangement offers prehensile manipulation via sensor-based motion manipulation strategies with flexible and electroelastic proprioceptive sensor plans [29]–[32]. By this, we mean the mechanical interactions of pushing or releasing by the IABs may be harnessed to further improve head manipulation robustness [33]–[35]. Explorative robotic positioning research studies have demonstrated the feasibility of maintaining stable patient cranial motion consistent with treatment plans using rigid Stewart-Gough platforms [36]–[38]. These achieve a $\leq 0.5\text{mm}$ and $\leq 0.5^\circ$ positioning accuracy 90% of the time. While aiding better clinical accuracy, they utilize rigid metallic components, electric motors and linear actuators which are not suitable for MRI imaging: they interfere with the magnets of the MRI machine, and can lead to patient fatality or significant damage to the MRI machine [39]. Time-resolved MRI techniques, which provide superior soft tissues image scans, can provide soft tissues delineation for use in brain or head and neck (H&N) radiation therapy (RT) [40]–[43]. Existing frame-based and frameless and maskless robotic motion correction mechanisms are not suitable for this because of their electro-mechanical parts that introduce radiation-attenuation and magnetic compliance concerns.

Pneumatic soft robots generally consist of a single structure with embedded actuators. However, when assembled, the region where the assemblies are connected easily undergoes large stress concentration which leads to failure. To overcome this issue, we have developed a hybrid actuator module that combines a soft actuation structure and rigid joining methods. Because the modules push each other through a rigid surface, the actuator can display good force transmission performance while maintaining high degrees of freedom (DOF) when

TABLE I: Common notations

Notation	Definition
B	An open set of particles on a Body, B
\mathbf{F}	The deformation gradient tensor, $\mathbf{F} = \nabla \chi_k(\mathbf{X}) = \dot{\mathbf{x}}_k(\mathbf{X})$.
$\boldsymbol{\sigma}$	The Cauchy stress tensor.
\mathbf{C}	The right Cauchy-Green tensor, $\mathbf{C} = \mathbf{F}^T \mathbf{F}$.
\mathbf{B}	The left Cauchy-Green tensor, $\mathbf{B} = \mathbf{F} \mathbf{F}^T$.
$\mathbf{v}(\mathbf{x})$	The velocity field $\dot{\mathbf{x}}(\mathbf{x}) = \dot{\mathbf{x}}(\mathbf{x}^{-1}(\mathbf{X}))$, where without loss of generality, we have taken $X = \mathbf{X}$, i.e. the place of X .

passively bent or twisted.

III. DEFORMATION ANALYSIS

Suppose that at rest, the IAB occupies a stress-free reference configuration \mathcal{B}_0 with boundary $\delta\mathcal{B}_0$ when no mechanical loads are present. Upon the application of a mechanical load, deformation occurs so that the body is transformed into a new configuration \mathcal{B} with boundary $\delta\mathcal{B}$. Material points in \mathcal{B}_0 are denoted by position vectors \mathbf{X} and they have a correspondence in configuration \mathcal{B} as \mathbf{x} . We assume regularity in the deformation from \mathcal{B}_0 to \mathcal{B} , denoted by χ such that $\mathbf{x} = \chi(\mathbf{X}, t)$. In the Lagrangean configuration, we define the deformation tensor as $\mathbf{F} = \text{Grad } \chi$ with Grad being the gradient operator acting on the material points, \mathbf{X} , in the configuration \mathcal{B}_0 . The common notations throughout the rest of this article are as defined in Table I. We work from a continuum mechanics framework, whereby we consider only final configurations of the soft actuators; thus we drop the explicit dependence of a configuration on time and rather write it as $\chi(\mathbf{X})$. For a background material on this section, we refer readers to [25, §2–§3] and [44].

A. Strain Analysis: The Deformation Gradient

The physical texture of the deformed IAB material is a hemisphere constrained along the polar direction, we choose spherical polar coordinates (r, θ, ϕ) , where r represents the radial distance of the particle from a fixed origin, θ is the azimuth angle on a reference plane through the origin and orthogonal to the polar angle, ϕ (where our notation follows that of [45]). Denote the internal and external radii as r_i , and r_o respectively with current/reference configuration

constraints (since radial symmetry is preserved throughout deformation as seen in Fig. 5),

$$\begin{aligned} r_i \leq r \leq r_o, \quad 0 \leq \theta \leq 2\pi, \quad 0 \leq \phi \leq \pi/2 \\ R_i \leq R \leq R_o, \quad 0 \leq \Theta \leq 2\pi, \quad 0 \leq \Phi \leq \pi/2. \end{aligned} \quad (1)$$

The position vectors in either configurations are

$$\mathbf{R} = \begin{pmatrix} X \\ Y \\ Z \end{pmatrix} = \begin{pmatrix} R \cos \Theta \sin \Phi, \\ R \sin \Theta \sin \Phi, \\ R \cos \Phi \end{pmatrix} \text{ and} \quad (2)$$

$$\mathbf{r} = \begin{pmatrix} x \\ y \\ z \end{pmatrix} = \begin{pmatrix} r \cos \theta \sin \phi, \\ r \sin \theta \sin \phi, \\ r \cos \phi \end{pmatrix}. \quad (3)$$

Given the incompressibility of the IAB material, the material volume contained between the IAB walls (of radii R_o and R_i respectively) remains constant throughout deformation, i.e. $\frac{2}{3}\pi(R^3 - R_i^3)$, equal in volume to $\frac{2}{3}\pi(r^3 - r_i^3)$ so that

$$r^3 = R^3 + r_i^3 - R_i^3, \quad \phi = \Phi. \quad (4)$$

For bases $\{\mathbf{e}_x\}$ and $\{\mathbf{e}_X\}$ (with respect to an observer) in the current and reference configurations respectively, we introduce the gradient operator, ∇ , (in the Lagrangean axes) for a fiber element $\mathbf{dx} = \mathbf{dx}_r \mathbf{e}_r + \mathbf{dx}_\phi \mathbf{e}_\phi$ (in Eulerian axes) so that

$$\nabla = \mathbf{e}_R \frac{\partial}{\partial R} + \mathbf{e}_\Phi \frac{1}{R} \frac{\partial}{\partial \Phi} + \mathbf{e}_\Theta \frac{1}{R \sin \Phi} \frac{\partial}{\partial \Theta}. \quad (5)$$

The deformation gradient, \mathbf{F} , as a *dyadic product* of a material line element in the current configuration and the gradient operator (5) is

$$\begin{aligned} \mathbf{F} &= \mathbf{dx} \otimes \nabla \\ &= (\mathbf{dx}_r \mathbf{e}_r + \mathbf{dx}_\phi \mathbf{e}_\phi + \mathbf{dx}_\theta \mathbf{e}_\theta) \otimes \\ &\quad \left(\mathbf{e}_R \frac{\partial}{\partial R} + \mathbf{e}_\Phi \frac{1}{R} \frac{\partial}{\partial \Phi} + \mathbf{e}_\Theta \frac{1}{R \sin \Phi} \frac{\partial}{\partial \Theta} \right). \end{aligned} \quad (6)$$

We can verify that the following deformation gradient relation holds

$$\mathbf{F} = \begin{pmatrix} \frac{R^2}{r^2} & 0 & 0 \\ 0 & \frac{r}{R} & 0 \\ 0 & 0 & \frac{r}{R} \end{pmatrix} \quad (7)$$

with principal stretches,

$$\lambda_r = \frac{R^2}{r^2}; \quad \lambda_\phi = \frac{r}{R}; \quad \lambda_\theta = \frac{r}{R} \quad (8)$$

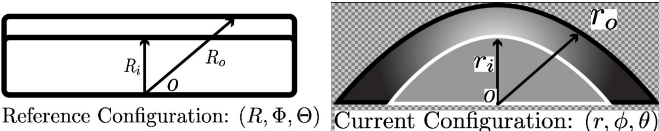


Fig. 5: Radii change under deformation.

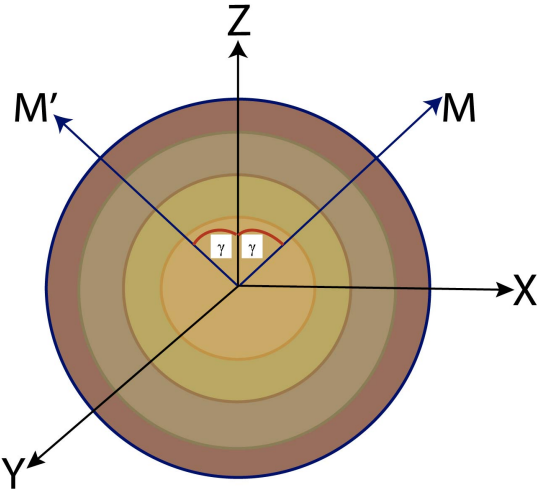


Fig. 6: A rubber strip reinforced by radially symmetric circular membranes along directions M and M' .

and associated right and left Cauchy-Green tensors are

$$\mathbf{C} = \mathbf{F}^T \mathbf{F}, \quad \mathbf{B} = \mathbf{FF}^T \quad (9a)$$

$$\mathbf{C} = \mathbf{B} = \begin{pmatrix} \frac{R^4}{r^4} & 0 & 0 \\ 0 & \frac{r^2}{R^2} & 0 \\ 0 & 0 & \frac{r^2}{R^2} \end{pmatrix}. \quad (9b)$$

B. Nonlinear Elastic Deformation Model

As we are dealing with air in the enclosure of the IAB, we use the Eulerian specification in our stress field equations. Forces that produce deformations are derived using the strain energy-invariants relationship, i.e., $\frac{\partial \Psi}{\partial I_1}$, $\frac{\partial \Psi}{\partial I_2}$ and $\frac{\partial \Psi}{\partial I_4}$. For readers implementing these on solids or hyperelastic materials, a Lagrangean formulation may be appropriate since a reference configuration may be chosen to coincide with the geometry of the solid initially. The elastic properties of the elastomer and fiber reinforcing are described in terms of the strain-energy functions Ψ_{iso} and Ψ_{mesh} respectively. Choosing a Mooney-Rivlin formulation [46], [47], we let the elastomer energy, Ψ_{iso} , depend on the invariants I_1 , and I_2 , functions of the principal stretches, $\lambda_r, \lambda_\phi, \lambda_\theta$ i.e.,

$$\begin{aligned} I_1 &= \mathbf{tr}(\mathbf{C}) = \lambda_r^2 + \lambda_\phi^2 + \lambda_\theta^2, \quad \text{and} \\ I_2 &= \mathbf{tr}(\mathbf{C}^{-1}) = \lambda_r^{-2} + \lambda_\phi^{-2} + \lambda_\theta^{-2}, \end{aligned} \quad (10)$$

where $\lambda_r \lambda_\phi \lambda_\theta = 1$ following the incompressibility assumption of the elastomeric IAB material. The Mooney-Rivlin strain energy for small deformations as a function of the strain invariants (10) is

$$\Psi = \frac{1}{2} C_1(I_1 - 3) + \frac{1}{2} C_2(I_2 - 3), \quad (11)$$

IAB material moduli.

Let us consider a strip of the IAB material in the axial plane with the three families of fibers that are symmetrically

²The subscripts r, ϕ , and θ denote the coordinates of a point on the actuator's body.

arranged with respect to the axes, as illustrated in Fig. 6. The fiber membrane's strain energy is constrained along the circumferential direction \mathbf{M}_i , for $i = 1, \dots, 3$ and the matrix form of each fiber position \mathbf{M}_i is

$$\mathbf{M}_i = [r_j, r_j, 0]^T, \quad (12)$$

where for the two outermost fibers, $r_j = r_{ext} - r_{int}$, and r_{ext}, r_{int} are respectively the external and internal radii of the fibers. If there is a deformation, we must have $\mathbf{m} = \mathbf{F}\mathbf{M}$ so that the standard reinforcing invariant I_4 can be written as

$$I_4 = \sum_{j=1}^3 \mathbf{M}_j \cdot \mathbf{C} \mathbf{M}_j \quad (13)$$

where the symbol “.” denotes the dot product and we choose the standard strain energy reinforcing model,

$$\Psi_{\text{mesh}}(I_4) = \frac{C_4}{2}(I_4 - 1)^2 \quad (14)$$

where C_4 is the fiber stiffness. Since the material to be incompressible ($J \equiv \det \mathbf{F} = 1$), the total strain energy of the elastomer-fiber composite is

$$\Psi(I_1, I_2, I_4) = \Psi_{\text{iso}}(I_1, I_2) + \Psi_{\text{mesh}}(I_4). \quad (15)$$

C. Stress Response from Strain Energy

We are concerned with the magnitudes of the differential stress on the IAB shells from a mechanical point of view and *our approach is based on a continuum mechanics viewpoint which is independent of finite element methods*. The IAB material stress response, \mathbf{G} , at any point on the IAB's boundary at time t determines the Cauchy stress, σ , as well as the history of the motion up to and at the time t [44]. The *constitutive equation* that relates the stress to an arbitrary motion will be determined using [48]'s *determinism for the stress principle*. The constitutive relation for the nominal stress deformation for an elastic IAB material is given by

$$\sigma = \begin{pmatrix} \sigma_{rr} & \sigma_{r\phi} & \sigma_{r\theta} \\ \sigma_{\phi r} & \sigma_{\phi\phi} & \sigma_{\phi\theta} \\ \sigma_{\theta r} & \sigma_{\theta\phi} & \sigma_{\theta\theta} \end{pmatrix} = \mathbf{G}(\mathbf{F}) + q\mathbf{F} \frac{\partial \Lambda}{\partial \mathbf{F}}(\mathbf{F}), \quad (16)$$

where \mathbf{G} is a functional with respect to the configuration χ , q acts as a Lagrange multiplier, and Λ denotes the internal (incompressibility) constraints of the IAB system. For an incompressible material, the indeterminate Lagrange multiplier becomes the hydrostatic pressure *i.e.* $q = -p$ [49]. The incompressibility of the IAB material properties imply that $\Lambda \equiv \det \mathbf{F} - 1$. We can verify that

$$\sigma = \mathbf{G}(\mathbf{F}) - p\mathbf{I} \quad (17)$$

since $\det(\mathbf{F}) = 1$. In terms of the stored strain energy, we find that

$$\sigma = \frac{\partial \Psi}{\partial \mathbf{F}} \mathbf{F}^T - p\mathbf{I} \quad (18)$$

where \mathbf{I} is the identity tensor and p represents an arbitrary hydrostatic pressure. It follows that the constitutive law that governs the Cauchy stress tensor is

$$\begin{aligned} \sigma &= \frac{\partial \Psi_{\text{iso}}}{\partial I_1} \frac{\partial I_1}{\partial \mathbf{F}} \mathbf{F}^T + \frac{\partial \Psi_{\text{iso}}}{\partial I_2} \frac{\partial I_2}{\partial \mathbf{F}} \mathbf{F}^T + \frac{\partial \Psi_{\text{mesh}}}{\partial I_4} \frac{\partial I_4}{\partial \mathbf{F}} \mathbf{F}^T - p\mathbf{I} \\ &= \frac{1}{2} C_1 \frac{\partial \text{tr}(\mathbf{FF}^T)}{\partial \mathbf{F}} \mathbf{F}^T + \frac{1}{2} C_2 \frac{\partial \text{tr}([\mathbf{F}^T \mathbf{F}]^{-1})}{\partial \mathbf{F}} \mathbf{F}^T \\ &\quad + C_4(I_4 - 1) \left[\frac{\partial \left(\sum_{j=1}^3 \mathbf{M}_j \cdot \mathbf{C} \mathbf{M}_j \right)}{\partial \mathbf{F}} \right] \mathbf{F}^T - p\mathbf{I} \\ &= C_1 \mathbf{FF}^T - C_2 (\mathbf{F}^T \mathbf{F})^{-1} + \\ &\quad 2C_4(I_4 - 1) \left[\sum_{j=1}^3 \mathbf{m}_j \otimes \mathbf{m}_j \right] - p\mathbf{I} \\ \sigma &= C_1 \mathbf{B} - C_2 \mathbf{C}^{-1} + 2C_4(I_4 - 1) \left[\sum_{j=1}^3 \mathbf{m}_j \otimes \mathbf{m}_j \right] - p\mathbf{I}, \end{aligned} \quad (19)$$

where $\mathbf{m}_j = \mathbf{F}\mathbf{M}_j$ and again \otimes represents the dyadic product of the respective tensors. Expanding (19), we see that the shear stresses vanish and we are left with the *relevant* normal stresses, given by

$$\sigma_{rr} = C_1 \lambda_r^2 - \frac{C_2}{\lambda_r^2} + 2C_4 \lambda_r^2 \sum_{j=1}^3 r_j^2 \left(\lambda_r^2 \sum_{j=1}^3 r_j^2 - 1 \right) - p, \quad (20a)$$

$$\sigma_{\phi\phi} = C_1 \lambda_\phi^2 - \frac{C_2}{\lambda_\phi^2} + 2C_4 \lambda_\phi^2 \sum_{j=1}^3 r_j^2 \left(\lambda_\phi^2 \sum_{j=1}^3 r_j^2 - 1 \right) - p, \quad (20b)$$

$$\sigma_{\theta\theta} = C_1 \lambda_\theta^2 - \frac{C_2}{\lambda_\theta^2} + 2C_4 \lambda_\theta^2 \sum_{j=1}^3 r_j^2 \left(\lambda_\theta^2 \sum_{j=1}^3 r_j^2 - 1 \right) - p. \quad (20c)$$

D. Boundary-Value Problem of Traction

The dynamic problem is to find the stress at every point in the robot's body subjected to external forces under suitable boundary conditions. Body forces are apply only along the axial direction; the fixed direction of axial loading implies that the deformation is a function of conservative forces only so that uniqueness of solution of stress field equations are preserved owing to Kirchoff's theorem [50, §7.4]. Furthermore, we assume that the applied pressure does not exceed a threshold that makes the rubber material yield to the point of buckling. The equilibrium equations for the physical component vectors of the body force, $\mathbf{b} = \{b_r, b_\phi\}$ are (see [24])

$$-b_r = \frac{1}{r^2} \frac{\partial(r^2 \sigma_{rr})}{\partial r} + \frac{1}{r \sin \phi} \frac{\partial(\sin \phi \sigma_{r\phi})}{\partial \phi} - \frac{1}{r} (\sigma_{\phi\phi} + \sigma_{\theta\theta}) \quad (21a)$$

$$-b_\phi = \frac{1}{r^3} \frac{\partial(r^3 \sigma_{r\phi})}{\partial r} + \frac{1}{r \sin \phi} \frac{\partial(\sin \phi \sigma_{\phi\phi})}{\partial \phi} - \frac{\cot \phi}{r} \sigma_{\theta\theta}. \quad (21b)$$

Owing to the symmetry of the elastic-fiber material, the shearing stresses vanish. We prescribe the following boundary conditions for the radial normal stress

$$\sigma_{rr}|_{r=r_o} = -P_{atm}, \quad \sigma_{rr}|_{r=r_i} = -P_{atm} - P \quad (22)$$

where P_{atm} is the atmospheric pressure and $P > 0$ is the internal pressure exerted on the walls of the IAB above P_{atm} i.e., $P > P_{atm}$. Thus, (21) becomes

$$-b_r = \frac{1}{r^2} \frac{\partial(r^2 \sigma_{rr})}{\partial r} - \frac{\sigma_{\phi\phi} + \sigma_{\theta\theta}}{r} \quad (23a)$$

$$-b_\phi = \frac{1}{r \sin \phi} \frac{\partial}{\partial \phi} (\sin \phi \sigma_{\phi\phi}) - \frac{\cot \phi}{r} \sigma_{\theta\theta}. \quad (23b)$$

Expanding (23a), we have

$$\frac{\partial \sigma_{rr}}{\partial r} = \frac{1}{r} (2\sigma_{rr} - \sigma_{\phi\phi} - \sigma_{\theta\theta} + rb_r). \quad (24)$$

We can find an expression for the hydrostatic pressure p by manipulating (20)a as follows

$$\frac{dp}{dr} = \frac{d}{dr}(\sigma_{rr} + p) - \frac{d\sigma_{rr}}{dr} \quad (25)$$

so that with the second boundary condition in (22), we have

$$p = -P - P_{atm} = (\sigma_{rr} + p) - \int_{r_i}^r \frac{\partial \sigma_{rr}}{\partial r} dr \quad (26)$$

or

$$p = P + C_1 \lambda_r^2 - \frac{C_2}{\lambda_r^2} + 2C_4 \lambda_r^2 \sum_{j=1}^3 r_j^2 \left(\lambda_r^2 \sum_{j=1}^3 r_j^2 - 1 \right) - \int_{r_i}^r \frac{1}{r} (2\sigma_{rr} - \sigma_{\phi\phi} - \sigma_{\theta\theta} + rb_r) dr \quad (27)$$

where without loss of generality, we may take $P_{atm} = 0$. Using the first boundary condition in (22), we can verify from (24) that

$$-P = \sigma_{rr}(r_i) = \int_{r_i}^{r_o} \frac{1}{r} (2\sigma_{rr} - \sigma_{\phi\phi} - \sigma_{\theta\theta} + rb_r) dr \quad (28)$$

where r , and b_r are known and σ_{rr} , $\sigma_{\phi\phi}$, and $\sigma_{\theta\theta}$ are given by (20). Under the incompressibility properties of the IAB material we have,

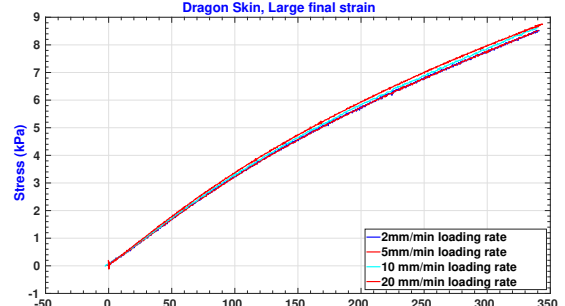
$$r^3 = R^3 + r_i^3 - R_i^3, \text{ and } r_o^3 = R_o^3 + r_i^3 - R_i^3. \quad (29)$$

Soft IK: Internal and Hydrostatic Pressure

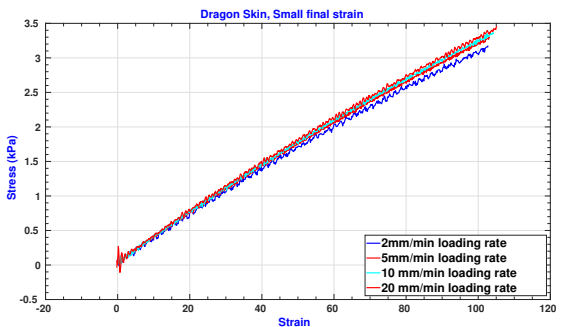
$$P = - \int_{r_i}^{r_o} \frac{1}{r} (2\sigma_{rr} - \sigma_{\phi\phi} - \sigma_{\theta\theta} + rb_r) dr \quad (30)$$

$$p = P + C_1 \lambda_r^2 - \frac{C_2}{\lambda_r^2} + 2C_4 \lambda_r^2 \sum_{j=1}^3 r_j^2 \left(\lambda_r^2 \sum_{j=1}^3 r_j^2 - 1 \right) - \int_{r_i}^r \frac{1}{r} (2\sigma_{rr} - \sigma_{\phi\phi} - \sigma_{\theta\theta} + rb_r) dr.$$

Furthermore, since the polar component of the normal stress is zero by reason of the fiber constraint, there is no loss in taking $\sigma_{\theta\theta} = 0$ in (30). Equations (28), and (29) completely determine the inverse kinematics (SOFT IK) of the



(a) Large final strain



(b) Small final strain.

Fig. 7: Stress-Strain Curves at large and small final strains respectively.

IAB material: for a required deformation, it determines the internal pressurization or normal Cauchy stress required to achieve a particular radial stretch.

E. Experimental Validation

We simplify the challenge of constructing a strain field based on a desired eventual shape by setting the undeformed membrane to a plane sheet as highlighted in the mechanical design section. In spherical polar coordinates, and in the reference configuration, ($R = \epsilon$)³ and the deformation is constrained so that there is no circumferential strain i.e. ($\Theta = 0$), so that the the deformation gradient, and left and right Cauchy-Green tensors of § III-A (7) becomes

$$\mathbf{F} = \begin{pmatrix} \frac{R^2}{r^2} & 0 \\ 0 & \frac{r}{R} \end{pmatrix}; \quad \mathbf{C} = \mathbf{B} = \begin{pmatrix} \frac{R^4}{r^4} & 0 \\ 0 & \frac{r^2}{R^2} \end{pmatrix} \quad (31)$$

1) *Material Moduli:* We carried out tensile testing experiments on a fabricated dragon skin (DS-10 Medium with shore hardness 10A) material using the Instron® tensile testing machine. We mix the A and B samples of the DS-10M material to form a rectangular fiber of size, $58.32 \times 38.44\text{mm}$. For different loading rates and at a large or small final strain, the stress-strain curves are as illustrated in Fig. 7.

2) *Material moduli and stiffness:* : The Mooney-Rivlin strain form allows the choice of any material moduli C_1, C_2 for the elastomer and C_4 for the fiber as illustrated in (15). In the deformation of our elastic-fiber matrices, the inflation and deflation regimes respond differently to different applied compressed air forces. In this regard, we chose C_1 to represent

³ ϵ is a very small positive number

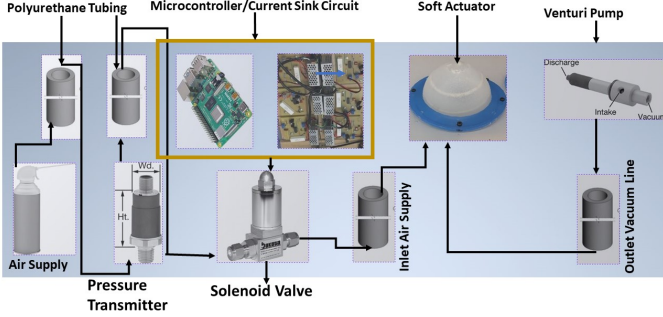


Fig. 8: Schematic of actuation mechanism.

the Young's modulus of the elastic material, as indicated in the slope of the graph in Fig. 7, and C_2 as the Poisson's ratio of an ideal incompressible rubber was chosen as $C_2 \sim 0.49$. For the concentric rings of nonwoven mesh that were embedded within the elastomer, we choose the elastic modulus of the fiber material that resists stretching as $C_4 \sim 7.7$ MPa similar to [27].

3) Soft IK Validation:

IV. CONTACT KINEMATICS

The interactions among the actuators and head is considered as a classical case of elastic bodies in contact. We describe the contact between an IAB and the head through a mapping between the force exerted by the IAB at the contact point and the resultant forces at the center of mass of the head. We use the *frictionless point contact* model [51] as our primitive contact configuration: forces are only applied in the direction normal to the surface of the actuator (in the axial direction), and the wrench convex has a single wrench such that the line of action going through the point of the contact and with direction the negative of the contact normal. The trajectory of the head under the influence of motion of an IAB is influenced by the position vector \mathbf{r} of (??). When the IAB deforms, body forces in its current configuration and the *traction* over its boundary $\partial\mathcal{B}$ impact motion on the head. We define the point contact force as

$$\tilde{\mathbf{F}}_{c_i} = \begin{pmatrix} n_{c_i} \\ \mathbf{0} \end{pmatrix} f_{c_i}, \quad (32)$$

where $f_{c_i} \in \mathbb{R}$ denotes the amount of force exerted by an actuator along the direction of contact, $n_{c_i} \in \mathbb{R}^3$. The head force and the contact force are related as $\tilde{\mathbf{F}}_o = \tilde{\mathbf{F}}_{c_i}$, and n_{c_i} is the *normal* or *Gauss map*⁴ for a manifold $S \subset \mathbb{R}^3$ of a head surface.

A. Contact/Traction Forces and Stress Equivalence

We assume that the stress vector σ at a point on the IAB surface is uniform and continuous throughout the IAB boundary so that it linearly depends on the normal map (this follows from Cauchy's theorem; readers may see the proof

⁴A normal map for a manifold S is a continuous map $g : S \rightarrow S^2 \subset \mathbb{R}^3$ such that for every $s \in S$, $g(s)$ is orthogonal to S at s [52].

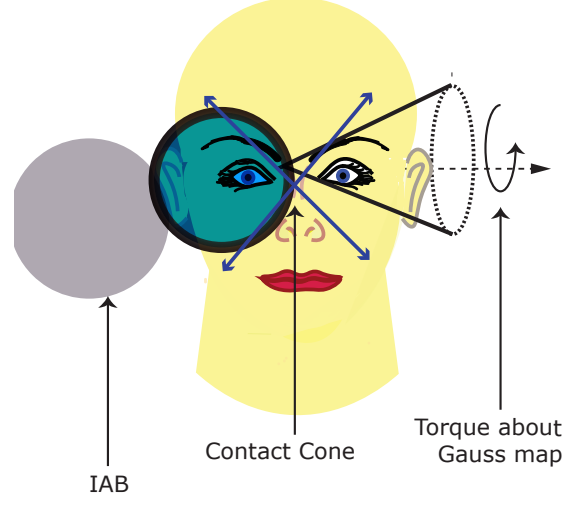


Fig. 9: Soft Contact Illustration

in [44, §3.3.1]). The correspondence between material line elements, $\{\mathbf{dx}, \mathbf{dX}\}$, in the reference and current configuration is

$$\mathbf{dx} = \mathbf{F} \mathbf{dX} \implies \mathbf{F}^{-T} \mathbf{dx} = \mathbf{dX}. \quad (33)$$

where \mathbf{F} is the deformation gradient.

Let $\mathbf{H} = \mathbf{F}^{-T}$ and \mathbf{da} represent an infinitesimal vector element on the material surface at a neighborhood of point \mathbf{X} in \mathcal{B} such that $\mathbf{da} = n_{c_i} da$. The corresponding deformed surface of the IAB with normal n_{c_i} from a surface, da , of the IAB in a configuration \mathcal{B} is $\mathbf{da} = n_{c_i} da$. Using *Nanson's formula*, we have the following relation between surfaces in the reference and current configuration

$$\mathbf{da} = J \mathbf{H} \mathbf{dA} \implies n_{c_i} da = J \mathbf{H} \mathbf{N} dA \quad (34)$$

where $J = \det \mathbf{F}$ and \mathbf{N} is the normal map in the reference configuration. On the bounding surface of the i 'th IAB the exerted force on a surface area \mathbf{da} in global form is

$$\mathbf{f}_{c_i} = \int_{\partial\mathcal{B}} \boldsymbol{\sigma} n_{c_i} da_i = \int_{\partial\mathcal{B}} (\sigma_{rr_i} + \sigma_{\phi\phi_i}) n_{c_i} da_i. \quad (35)$$

Owing to the isochoric assumption, the force is uniform throughout the boundary of the IAB body so that we have,

$$\tilde{\mathbf{F}}_{c_i} = (\sigma_{rr_i} + \sigma_{\phi\phi_i}) n_{c_i} a_i \quad (36)$$

where a_i is the cross-sectional area of the actuator when in contact with the head.

B. Contact Coordinates and Head Velocity

The head will make contact with the IAB at multiple points on its surface, so we describe the kinematics of these contact

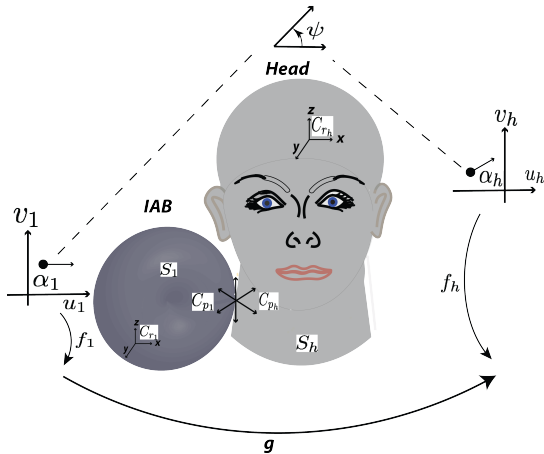


Fig. 10: Sliding and rolling contact illustration of a single IAB and the Head. [Image best visualized in colored ink].

points using an atlas⁵ of contact coordinate charts. In this sentiment, let C_{r_1} and C_{r_h} respectively represent a fixed reference frame with respect to the IAB and head, H respectively (see Fig. 10). Furthermore, let $S_1 \subset \mathbb{R}^3$ and $S_h \subset \mathbb{R}^3$ denote the respective orientable manifold⁶ embeddings of the IAB and head surfaces with respect to frames C_{r_1} and C_{r_h} . We shall let S_1 and S_h belong to the atlases $\{S_{1_i}\}_{i=1}^{n_1}$, $\{S_{h_i}\}_{i=1}^{n_h}$ respectively. Suppose (f_1, U_1) and (f_h, U_h) are coordinate systems for the IAB and the head respectively, where f_i is an invertible map, $f_i(u_i, v_i) : U \rightarrow S_i \subset \mathbb{R}^3$

$$f_i(u_i, v_i) : \{U \rightarrow S_i \subset \mathbb{R}^3 | i = 1, h\},$$

from an open subset U of \mathbb{R}^2 to a coordinate patch $S_i \subset \mathbb{R}^3$ such that the partial derivatives $\frac{\partial f_i}{\partial u_i}$ and $\frac{\partial f_i}{\partial v_i}$ are linearly independent. Let $p_1(t) \in S_1$ and $p_h(t) \in S_h$ represent the positions of the contact points with respect to frames C_{r_1} and C_{r_h} respectively at time t . In general, the contact points $p_1(t)$ and $p_h(t)$ will not remain in the coordinate systems S_1 and S_h for all time. Thus, we choose an interval I where $p_1(t) \in S_{1_i}$ and $p_h(t) \in S_{h_j}$ for all $t \in I$ and some i and j . As seen in Fig. 10, C_{p_1} and C_{p_h} denote the contact frames that coincide with the normalized Gauss frames at p_1 and p_h for all $t \in I$, and α_1 , α_h are local coordinate frames that describe the IAB motion with respect to the head such that

$$\alpha_1 = (u_1, v_1) \in U_1, \text{ and } \alpha_h = (u_h, v_h) \in U_h. \quad (37)$$

Let the angle between the tangent planes of α_1 , and α_h be ψ . The transformation matrix $g \in \Omega \subset SE(3)$ encodes the relative orientation and position of the IAB with respect to the head, where Ω is the set of all relative positions and orientations in the atlases $\{S_{1_i}\}_{i=1}^{n_1}$, $\{S_{h_i}\}_{i=1}^{n_h}$ for which the IAB and head remain in contact. We let the contact coordinates be described by $\eta = (\alpha_1, \alpha_h, \psi)$. The head's motion is governed by traction

⁵An atlas \tilde{S} is a set of surfaces where each surface $S \in \tilde{S}$ has an invertible map $f(\mathbf{u})$ from an open subset U of \mathbb{R}^2 to a surface $S \subset \mathbb{R}^3$ such that the partial derivatives $\frac{\partial f}{\partial u}(\mathbf{u}), \frac{\partial f}{\partial v}(\mathbf{v})$ are linearly independent for all $\mathbf{u} = (u, v) \in U$.

⁶An orientable manifold is a manifold S for which the Gauss map exists.

forces arising from the friction tangential to the IAB surface and the pressure normal to the IAB surface. Thus, at the points of contact, if $R \in SO(3)$ is the rotational component of g , η must satisfy

$$g \circ f_1(\alpha_1) = f_h(\alpha_h) \quad (38a)$$

$$R n_1(\alpha_1) = -n_h(\alpha_h) \quad (38b)$$

since the contact locations must coincide for the IAB and the head, and the tangent planes must coincide so that the outward normal maps $n_1 : S_1 \rightarrow S^2 \subset \mathbb{R}^3$ and $n_h : S_h \rightarrow S^2 \subset \mathbb{R}^3$ agree. Furthermore, the orientation of the tangent planes of α_1 and α_h is the unique angle $\psi \in [0, 2\pi)$ between the x -axes of C_{p_1} and C_{p_h} such that

$$R \frac{\partial f_1}{\partial \alpha_1} M_1^{-1} R_\psi = \frac{\partial f_h}{\partial \alpha_h} M_h^{-1} \quad (39)$$

where M_i is a 2×2 square root of the Riemannian metric tensor [53] that normalizes the columns of $\frac{\partial f}{\partial \alpha}$, i.e.

$$M_i = \begin{bmatrix} \|\frac{\partial f_i}{\partial u_i}\| & 0 \\ 0 & \|\frac{\partial f_i}{\partial v_i}\| \end{bmatrix} \quad (40)$$

and R_ψ is chosen such that a rotation of C_{p_1} about its z -axis through $-\psi$ radians aligns the x -axes of the local coordinate system α_1 to that of the head's local coordinate system α_h i.e.

$$R_\psi = \begin{bmatrix} \cos \psi & -\sin \psi \\ -\sin \psi & \cos \psi \end{bmatrix} \quad (41)$$

with the special property that $R_\psi = R_\psi^T = R_\psi^{-1}$. We define the normalized Gauss frame at a point u on the surface U of the orthogonal coordinate system (f, U) as,

$$[x_u \ y_u \ z_u] = [\frac{\partial f}{\partial u} / \|\frac{\partial f}{\partial u}\| \ \ \frac{\partial f}{\partial v} / \|\frac{\partial f}{\partial v}\| \ \ n_u(f(u))] \quad (42)$$

where x_u , y_u , and z_u are functions mapping $U \subset \mathbb{R}^2 \rightarrow \mathbb{R}^3$ and n_u is the continuous Gauss map $n_u : S \rightarrow S^2 \subset \mathbb{R}^3$. The motion of the contacts $\dot{\eta}$ as a function of components of the twist vector $\hat{\xi} = (v, w)^T$ is given in (43) as the respective first, second, and third equations of contact. Our derivation, which closely follows [54]'s multi-fingered kinematics' proof, may be found in Appendix ??.

$$\dot{\alpha}_h = M_h^{-1} (\mathcal{K}_h + \tilde{\mathcal{K}}_1)^{-1} (\omega_t - \tilde{\mathcal{K}}_1 v_t) \quad (43a)$$

$$\dot{\alpha}_1 = M_1^{-1} R_\psi (\mathcal{K}_h + \tilde{\mathcal{K}}_1)^{-1} (\omega_t - \mathcal{K}_h v_t) \quad (43b)$$

$$\dot{\psi} = \omega_n + T_h M_h \dot{\alpha}_h + T_1 M_1 \dot{\alpha}_1 \quad (43c)$$

where

$$T_h = y_h^T \frac{\partial x_h}{\partial \alpha_h} M_h^{-1}, \quad T_1 = y_1^T \frac{\partial x_1}{\partial \alpha_1} M_1^{-1},$$

$$\mathcal{K}_h = [x_h^T, \ y_h^T]^T \frac{\partial n_h^T}{\partial \alpha_h} M_h^{-1}, \quad \omega_n = z_h^T \omega$$

$$\tilde{\mathcal{K}}_1 = R_\psi [x_1^T, \ y_1^T]^T \frac{\partial n_1^T}{\partial \alpha_1} M_1^{-1} R_\psi,$$

$$\omega_t = [x_h^T, \ y_h^T]^T [n_h \times \omega]^T,$$

$$v_t = [x_h^T, \ y_h^T]^T [(-f_h \times \omega + v)]^T. \quad (44)$$

Note that ω_t is the rolling velocity of the head projected onto the tangent plane of the contact and v_t is the sliding velocity; ω_n is the relative rotational velocity projected to the contact's surface normal, and $\tilde{\mathcal{K}}_1 = R_\psi \mathcal{K}_1 R_\psi$ is the curvature of the IAB with respect to the contact frame that coincides with the normalized Gauss frame at $p_1(t)$. The matrix $(\mathcal{K}_h + \tilde{\mathcal{K}}_1)^{-1}$ is the so-called *relative curvature* originally coined by [52]. Simplifying (44), we find that

$$\begin{aligned} x_h &= \frac{\partial f}{\partial u_h} / \left\| \frac{\partial f}{\partial u_h} \right\|, \quad y_h = \frac{\partial f}{\partial v_h} / \left\| \frac{\partial f}{\partial v_h} \right\|, \quad z_h = n_u(f(u)) \\ T_h &= y_h \left[\frac{\partial x_h^T}{\partial u_h} / \left\| \frac{\partial f}{\partial u_h} \right\|, \frac{\partial x_h^T}{\partial v_h} / \left\| \frac{\partial f}{\partial v_h} \right\| \right], \\ T_1 &= y_1 \left[\frac{\partial x_1^T}{\partial u_1} / \left\| \frac{\partial f}{\partial u_1} \right\|, \frac{\partial x_1^T}{\partial v_1} / \left\| \frac{\partial f}{\partial v_1} \right\| \right], \\ \mathcal{K}_h &= [x_h^T, \quad y_h^T]^T \left[\frac{\partial n_h^T}{\partial u_h} / \left\| \frac{\partial f}{\partial u_h} \right\|, \frac{\partial n_h^T}{\partial v_h} / \left\| \frac{\partial f}{\partial v_h} \right\| \right], \\ \mathcal{K}_1 &= [x_1^T, \quad y_1^T]^T \left[\frac{\partial n_1^T}{\partial u_1} / \left\| \frac{\partial f}{\partial u_1} \right\|, \frac{\partial n_1^T}{\partial v_1} / \left\| \frac{\partial f}{\partial v_1} \right\| \right]. \end{aligned} \quad (45)$$

We see that for the contact interaction between an IAB and the head, for a $U \subset \mathbb{R}^2$ we must choose an appropriate $f_i : U_i \rightarrow S_i \subset \mathbb{R}^3$ in order to characterize the setup.

V. SYSTEM'S NEWTON-EULER EQUATIONS

From Truesdell's *determinism for the stress principle* [48], the Cauchy stress σ at any point in a material at time t for any motion up to time t determines the stress response of the material for any arbitrary motion history up to and including time t . We will derive the dynamics of the IAB system in the *strain field of the deformation*. The potential and kinetic energy of the system are considered to be derived from the constitutive strain field relations that characterize the deformation. We now use Lagrangian deformation analysis to derive the dynamic equations of the continuum multi-IAB system.

For a soft continuum body, there is an enormous amount of particle orientations during deformation; the number of particle states that is physically measurable with sensors instantaneously in a given configuration is overwhelming. However, we can leverage the constitutive law which describes the macroscopic IAB material behavior with respect to a reference frame, S , at a time, t by completely characterizing it by ten dependent variables viz., three components of the position vector, six component stress tensor variables (the shear and normal stress components), and

A. Lagrangian and Euler-Lagrange Equations

We are only interested in the final position and orientation of the IAB as a whole rather than the system of particles that characterize a deformation at every time t . When the head exerts a reactive wrench on an IAB, it is natural to expect a dent. The shear angle in (??) should capture the amount of angular deformation. For a kinetic energy T and a potential energy V , the *Lagrangian*, L , of the system in generalized coordinates is the difference between the kinetic and potential energy, *i.e.*

$$L(\mathbf{r}, \dot{\mathbf{r}}) = T(\mathbf{r}, \dot{\mathbf{r}}) - V(\mathbf{r}). \quad (46)$$

The equations of motion for a pneumatic IAB system is of the form

$$\frac{d}{dt} \frac{\partial L}{\partial \dot{\mathbf{r}}_i} - \frac{\partial L}{\partial \mathbf{r}_i} = \boldsymbol{\tau}_i, \quad i = 1, \dots, m \quad (47)$$

where $\boldsymbol{\tau}_i$ is the torque acting on the i^{th} generalized coordinate. Written in matrix form equation, we can write the Euler-Lagrange equation of (47) as

$$\frac{d}{dt} \frac{\partial L}{\partial \dot{\mathbf{r}}} - \frac{\partial L}{\partial \mathbf{r}} = \boldsymbol{\tau}. \quad (48)$$

It now remains to derive the kinetic and potential energies for the IAB material. Let the velocity of an IAB material particle x in the current configuration at time t be $\mathbf{v}(\mathbf{r}, t)$, then the Eulerian velocity gradient tensor can be defined as

$$\boldsymbol{\Gamma} = \text{grad } \mathbf{v}(\mathbf{r}, t). \quad (49)$$

Cauchy's first law of motion [24, eq. 19] will allow us to derive the balance of mechanical energy of the system. Multiplying throughout by \mathbf{v} , we find that

$$\begin{aligned} \text{div} (\boldsymbol{\sigma}^T \cdot \mathbf{v}) + \rho \mathbf{b} \cdot \mathbf{v} &= \rho \mathbf{v} \cdot \dot{\mathbf{v}} \\ \text{or div} (\boldsymbol{\sigma}^T \mathbf{v}) - \text{tr}(\boldsymbol{\sigma} \boldsymbol{\Gamma}) + \rho \mathbf{b} \cdot \mathbf{v} &= \rho \mathbf{v} \cdot \dot{\mathbf{v}}. \end{aligned} \quad (50)$$

where ρ is the IAB's mass density. Following mass conservation, we integrate over volume \mathcal{B} and employ the divergence theorem, so that the above relation yields the *balance of mechanical energy*

$$\begin{aligned} \int_{\mathcal{B}} \rho \mathbf{b} \cdot \mathbf{v} dv + \int_{\partial \mathcal{B}} f_\rho \cdot \mathbf{v} da &= \frac{d}{dt} \int_{\mathcal{B}} \frac{1}{2} \rho \mathbf{v} \cdot \mathbf{v} dv \\ &\quad + \int_{\mathcal{B}} \text{tr}(\boldsymbol{\sigma} \boldsymbol{\Gamma}) dv \end{aligned} \quad (51)$$

where f_ρ is the IAB body force density, and the left hand side of the foregoing is the so-called *rate of working of the applied forces*. The symmetry of the stress tensor $\boldsymbol{\sigma}$ implies that $\text{tr}(\boldsymbol{\sigma} \boldsymbol{\Gamma}) = \text{tr}(\boldsymbol{\sigma} \boldsymbol{\Sigma})$ where $\boldsymbol{\Sigma}$ is given in terms of the Eulerian-strain rate tensor, $\boldsymbol{\Gamma}$ *i.e.*,

$$\boldsymbol{\Sigma} = \frac{1}{2} (\boldsymbol{\Gamma} + \boldsymbol{\Gamma}^T) \quad (52)$$

so that the kinetic energy density and stress power are

$$T(\mathbf{r}, \dot{\mathbf{r}}) = \frac{1}{2} \rho \mathbf{v} \cdot \mathbf{v}, \quad V(\mathbf{r}) = \text{tr}(\boldsymbol{\sigma} \boldsymbol{\Sigma}). \quad (53)$$

B. Case I: Euler-Lagrange Equation for Cauchy-Elastic IAB Material

The stress-strain relation for the IAB we have presented are only related through the deformation tensor, implying that the material is Cauchy elastic. For Cauchy elastic materials, the stress power term is not conserved during deformation making integration over the material body \mathcal{B} physically unrealistic [44]. For such materials, we may set the stored strain energy V to an arbitrary constant (*e.g.* $V(I) = 0$). We can derive the torque dynamics of an IAB actuator as (see proof in Appendix C)

$$\boldsymbol{\tau} = \rho \ddot{\mathbf{r}}. \quad (54)$$

Rewriting equation (54) in terms of the torque for each soft robot, we have the dynamics for IAB j as

$$M_{iab_j}(\mathbf{r}_j)\ddot{\mathbf{r}}_j + C_{iab_j}(\mathbf{r}_j, \dot{\mathbf{r}}_j)\dot{\mathbf{r}}_j = \boldsymbol{\tau}_j \quad (55)$$

where M_{iab_j} and C_{iab_j} contain the respective inertia and Coriolis forces for actuator j . Since the IAB material is incompressible, the mass density is uniform throughout the body of the material. In general, we write equation (55) as

$$\mathbf{M}_{iab}(\tilde{\mathbf{r}})\ddot{\tilde{\mathbf{r}}} + \mathbf{C}_{iab}(\tilde{\mathbf{r}}, \dot{\tilde{\mathbf{r}}})\dot{\tilde{\mathbf{r}}} = \tilde{\boldsymbol{\tau}} \quad (56)$$

where $\tilde{\mathbf{r}} \in \mathbb{R}^{n_1} \times \mathbb{R}^{n_2} \times \dots \mathbb{R}^{n_s}$ gives the generalized coordinates for all the IABs and $\tilde{\boldsymbol{\tau}}$ are the vectorized torques of the individual robots.

C. Case II: Euler-Lagrange Equation for Green Elastic IAB Material

For completeness, we treat the case where the IAB material body is *hyperelastic* (i.e., *Green elastic*)⁷, the eulerian form of the stress power expression is

$$V(\mathbf{r}) = \mathbf{tr}(\boldsymbol{\sigma} \boldsymbol{\Sigma}). \quad (57)$$

We are mostly interested in the mechanical energy in the current configuration, however, it is worthwhile to note that the equivalent relation in the Lagrangean form is

$$\begin{aligned} & \int_{\mathcal{B}_o} \rho_o \mathbf{b}_o \dot{\chi} dV + \int_{\partial \mathcal{B}_o} (\boldsymbol{\sigma}^T \mathbf{N}) \dot{\chi} dA = \\ & \frac{d}{dt} \int_{\mathcal{B}_o} \frac{1}{2} \rho_o \dot{\chi} \cdot \dot{\chi} dV + \int_{\mathcal{B}_o} \mathbf{tr}(\boldsymbol{\sigma} \dot{\mathbf{F}}) dV, \end{aligned} \quad (58)$$

It follows that,

$$V(\mathbf{r}) = \mathbf{tr}(\boldsymbol{\sigma} \dot{\mathbf{F}}) \quad (59)$$

for a Green elastic material. Similar to the arguments in § V-B, we find the torque as (see derivation in Appendix C)

Green-Elastic IAB Material Torque

$$\begin{aligned} \boldsymbol{\tau} = & \frac{\rho \ddot{r}}{R^2} + \rho \ddot{\alpha} + \frac{\rho \dot{r}^2}{R^3} + 4C_1 \left(\frac{2R^3}{r^5} + \frac{r}{R^3} \right) \\ & + 4C_2 \left(\frac{2r^3}{R^5} + \frac{R}{r^3} \right). \end{aligned} \quad (60)$$

VI. MULTI-IAB STATICS AND END-EFFECTOR VELOCITIES

Following the CCOARSE deformation model, the regularity of the IAB in its current configuration, $\chi(\mathbf{r}, t)$, implies that it can be uniformly defined by \mathbf{r} throughout the IAB material. Similar to our model in [24], we are interested in the final state of the IAB after deformation; the path it takes for us to reach the final configuration is not important to us (since there is no obstacle in the continuum robots' workspace). Thus we drop the time dependence on the configuration and take \mathbf{r} to be the generalized coordinate of the IAB. The configuration space of

⁷An hyperelastic material is one where the strain-energy function exists.

the IAB with respect to the spatial frame at a certain time can then be described by $g_{st}(\chi) \equiv g_{st}(\mathbf{r}) : \mathbf{r} \rightarrow g_{st}(\mathbf{r}) \in SE(3)$ while the strain state of the IAB is characterized by the strain field

$$\hat{\xi}_i(\mathbf{r}) = g_i^{-1} \frac{\partial g_i}{\partial \mathbf{r}} \in \mathfrak{se}(3) = g_i^{-1} g'_i \quad (61)$$

with the respective g'_i 's being the tangent vector at g_i such that $g'_i \in T_{g_i}(\mathbf{r})SE(3)$. Note that $T_{g_i}(\mathbf{r})$ is the tangent matrix at g_i with associated Lie algebra $se(3) \approx T_e SE(3)$.

A. End Effector Forces

From the derived relationship between the head contact coordinates and the relative motion (v_t, ω_t) of the IAB i.e. equation (43), we can associate a Jacobian that maps IAB velocities to head position and orientation. A fundamental assumption in our formulation is that the IABs make contact with the head throughout manipulation, and the manipulation is stable and prehensile. A forward kinematic map from the configuration of the i^{th} IAB, χ_{iab_i} maps from respective IAB configurations to head position and orientation i.e. $K_{iab_i} : \chi_{iab_i} \rightarrow SE(3)$. The velocity of the head with respect to a fixed base frame in terms of IAB velocities can be written in terms of the forward kinematics Jacobian:

$$\begin{pmatrix} v_{iab_i} \\ \omega_{iab_i} \end{pmatrix} = \frac{\partial K_{iab_i}}{\partial \mathbf{r}_i} \frac{d\mathbf{r}_i}{dt} K_{iab_i}^{-1} = \mathbf{J}_i(\mathbf{r}_i) \dot{\mathbf{r}}_i \quad (62)$$

where \mathbf{r}_i is the spatial position of IAB i , and $(v_{iab_i}^T, \omega_{iab_i}^T) \in \mathbb{R}^6$ represents the linear and angular velocity of the i^{th} IAB about its screw basis. In essence, $\mathbf{r}_i \in \mathbb{R}^3$ with its rows of mapped to scalars by an appropriate choice of norm. The contact between the head and the IABs is mapped by the Jacobian

$$\mathbf{J}_{c_i}(\xi_h, \xi_{iab_i}) = \begin{bmatrix} \mathbf{I} & \hat{w}(r_{c_i}) \\ \mathbf{0} & \mathbf{I} \end{bmatrix} J_{r_i}, \quad (63)$$

where $\mathbf{J}_{c_i} : \dot{\xi}_{r_i} \rightarrow [v_{c_i}^T, w_{c_i}^T]^T$, $r_{c_i} \in \mathbb{R}^3$ is a vector between the head reference point (e.g. the center of mass) and the contact with the i^{th} IAB, ξ_h is the position and relative orientation of the head, ξ_{iab_i} is the position and relative orientation of the i^{th} soft robot in world coordinates, $\hat{w}(r_{c_i})$ is an anti-symmetric matrix for the vector r_{c_i} , and $\xi_r = (\xi_{r_1}, \xi_{r_2}, \dots, \xi_{r_8})$ are the positions and orientations for each of the 8 IABs. The manipulation map, G_i is made up of matrices of the form

$$G_i(\xi_h, \xi_r) = \begin{bmatrix} \mathbf{I} & \mathbf{0} \\ \hat{w}(r_{c_i}) & \mathbf{I} \end{bmatrix} B_i(\xi_h, \xi_r), \quad (64)$$

where $B_i(\xi_h, \xi_r)$ is the selection map as defined in [55] for the desired manipulation. The net force on the head is a sum of the individual forces arising from each IAB. Owing to the linearity of each individual IAB's contact force, the resultant head force can be stitched together to form G , i.e.

$$\tilde{F}_h = [G_1, \dots, G_8] \begin{pmatrix} \tilde{F}_{c_1} \\ \vdots \\ \tilde{F}_{c_8} \end{pmatrix} = G \tilde{F}_c, \quad (65)$$

where $F_h \in \mathbb{R}^6$ and $F_c \in \mathbb{R}^{m_1} \times \mathbb{R}^{m_2} \times \dots \times \mathbb{R}^{m_s}$. The *internal* or *null forces* is captured by the null space $\mathcal{N}(G)$ of the manipulation map G ; these forces correspond to zero net force on the head of the patient. Each \tilde{F}_{c_i} in (65) is of the form (36).

B. End-effector Velocities

We define the velocity constraint dual of (64) as the constraint between the relative velocity of the head and that of the twist velocities of the contact point

$$\begin{pmatrix} \tilde{v}_{c_i} \\ \tilde{\omega}_{c_i} \end{pmatrix} = \begin{bmatrix} \mathbf{I} & \hat{\omega}(r_{c_i}) \\ 0 & \mathbf{I} \end{bmatrix} \begin{pmatrix} v_{c_h} \\ \omega_{c_h} \end{pmatrix}. \quad (66)$$

For a conjugate twist vector $(v_c^T, \omega_c^T)^T$ to the forces exerted by the IABs, f_c , we have the following

$$\begin{pmatrix} v_c \\ \omega_c \end{pmatrix} = G^T \begin{pmatrix} v_{c_h} \\ \omega_{c_h} \end{pmatrix}. \quad (67)$$

Given a *selection matrix* $B_i^T(\xi_h, \xi_{iab_i}) \in \mathbb{R}_i^m$ for a particular IAB, where m_i is the range of all the forces and moments for the chosen contact primitive (or union of contact primitives), the *manipulation map* for the i^{th} IAB can be written as,

$$G_i^T(\xi_h, \xi_{iab_i})\xi_h = B_i^T(\xi_h, \xi_{iab_i})\mathbf{J}_{c_i}(\xi_h, \mathbf{r}_{r_i})\dot{\xi}_{iab_i} \quad (68)$$

where \mathbf{J}_{c_i} is the contact Jacobian for the i^{th} actuator, and ξ_h denotes the velocity of the head. For the 8 soft actuators, the manipulation constraint of the system can be written as

$$\begin{bmatrix} G_1^T \\ G_2^T \\ \vdots \\ G_8^T \end{bmatrix} \begin{pmatrix} v_h \\ w_h \end{pmatrix} = \text{diag} \begin{pmatrix} B_1^T \mathbf{J}_{c_1} \\ B_2^T \mathbf{J}_{c_2} \\ \vdots \\ B_8^T \mathbf{J}_{c_8} \end{pmatrix} \begin{pmatrix} \dot{\mathbf{r}}_{iab_1} \\ \dot{\mathbf{r}}_{iab_2} \\ \vdots \\ \dot{\mathbf{r}}_{iab_8} \end{pmatrix}. \quad (69)$$

VII. NEWTON-EULER SYSTEM OF EQUATIONS

The dynamics of the head is a form of (56) but without the actuator torques. In local coordinates, it has the form

$$\mathbf{M}_h(\zeta)\ddot{\zeta} + \mathbf{C}_h(\zeta, \dot{\zeta})\dot{\zeta} + \mathbf{N}_h(\zeta, \dot{\zeta}) = 0 \quad (70)$$

with ζ being a local parameterization of the position and orientation of the head in the Lie Group $SE(3)$, and \mathbf{N}_h being the gravitational and frictional forces exerted by/on the head. The head and the multi-DOF IAB system are connected via the manipulation constraint *i.e.*

$$G^T(\zeta, \mathbf{r})\dot{\zeta} = \mathbf{J}(\zeta, \mathbf{r})\dot{\mathbf{r}}. \quad (71)$$

Suppose that the velocity constraint produces a virtual displacement constraint in $\delta\zeta$ and $\delta\mathbf{r}$ such that for $q = (\zeta, \mathbf{r})$, we have

$$\delta\mathbf{r} = \mathbf{J}^{-1}(q)G^T(q)\delta\zeta$$

the Lagrange equations become

$$\left(\frac{d}{dt} \frac{\partial L}{\partial \dot{q}} - \frac{\partial L}{\partial q} - (\boldsymbol{\tau}, 0) \right) \delta q = 0 \quad (72a)$$

$$\left(\frac{d}{dt} \frac{\partial L}{\partial \dot{\mathbf{r}}} - \frac{\partial L}{\partial \mathbf{r}} - \boldsymbol{\tau} \right)^T \begin{pmatrix} \delta\mathbf{r} \\ \delta\zeta \end{pmatrix} = 0 \quad (72b)$$

$$\left(\frac{d}{dt} \frac{\partial L}{\partial \dot{\mathbf{r}}} - \frac{\partial L}{\partial \mathbf{r}} - \boldsymbol{\tau} \right) \delta\mathbf{r} + \left(\frac{d}{dt} \frac{\partial L}{\partial \dot{\zeta}} - \frac{\partial L}{\partial \zeta} \right) \delta\zeta = 0 \quad (72c)$$

$$GJ^{-T} \left(\frac{d}{dt} \frac{\partial L}{\partial \dot{\mathbf{r}}} - \frac{\partial L}{\partial \mathbf{r}} - \boldsymbol{\tau} \right) \delta\zeta + \left(\frac{d}{dt} \frac{\partial L}{\partial \dot{\zeta}} - \frac{\partial L}{\partial \zeta} \right) \delta\zeta = 0 \quad (72d)$$

wherefore,

$$\left(\frac{d}{dt} \frac{\partial L}{\partial \dot{\zeta}} - \frac{\partial L}{\partial \zeta} \right) \delta\zeta + GJ^{-T} \left(\frac{d}{dt} \frac{\partial L}{\partial \dot{\mathbf{r}}} - \frac{\partial L}{\partial \mathbf{r}} \right) = GJ^{-T} \boldsymbol{\tau} \quad (73)$$

given the arbitrariness of $\delta\zeta$. Equations (73) alongside (71) completely describe the system dynamics. Putting (55) into (73), we have

$$\left(\frac{d}{dt} \frac{\partial L}{\partial \dot{\zeta}} - \frac{\partial L}{\partial \zeta} \right) \delta\zeta = GJ^{-T} \left(1 - \frac{\rho}{2\|\mathbf{r}\|^2} \right) \boldsymbol{\tau}. \quad (74)$$

VIII. CONCLUSIONS

We have presented the constitutive model of these new class of soft actuators and we have presented the kinematic and dynamic equations that govern the behavior of the soft mechanism under mechanical loads. Future work will integrate the hardware for the tasks so described herein. Furthermore, in a follow-up paper (to be released shortly), we prescribe a trajectory optimization algorithm that uses the presented model on several manipulation and control tasks.

REFERENCES

- [1] K. H. Hunt, *Kinematic Geometry of Mechanisms*. Oxford University Press, 1977. [1](#), [3](#), [14](#)
- [2] *Parallel robots*. Springer, 2015. [1](#)
- [3] J. K. Salisbury, “Kinematic and Force Analysis of Articulated Hands,” Ph.D. dissertation, Stanford University, 1982. [1](#)
- [4] R. M. Murray, *A Mathematical Introduction To Robotic Manipulation*. CRC press, 1994. [1](#)
- [5] T. George Thuruthel, Y. Ansari, E. Falotico, and C. Laschi, “Control Strategies for Soft Robotic Manipulators: A Survey,” *Soft Robotics*, vol. 5, no. 2, pp. 149–163, 2018. [1](#)
- [6] Burridge, R R and Rizzi, A A and Koditschek, D E, “Sequential Composition of Dynamically Dexterous Robot Behaviors, Tech. Rep. 6, 1999. [1](#)
- [7] O. Ogunmolu, A. Kulkarni, Y. Tadesse, X. Gu, S. Jiang, and N. Gans, “Soft-NeuroAdapt: A 3-DOF Neuro-Adaptive Patient Pose Correction System for Frameless and Maskless Cancer Radiotherapy,” in *IEEE/RSJ International Conference on Intelligent Robots and Systems (IROS), Vancouver, BC, CA*. IEEE, 2017, pp. 3661–3668. [1](#), [2](#)
- [8] V. Gough, “Contribution to discussion of papers on research in automobile stability, control and tyre performance,” *Proc. of Auto Div. Inst. Mech. Eng.*, vol. 171, pp. 392–395, 1957. [1](#)
- [9] Neuman, Karl-Erik, “Robot,” Patent 4,732,525, March, 1988. [1](#)
- [10] P. Nanua and K. J. Waldron, “Direct Kinematic Solution of a Stewart platform,” in *1989 IEEE International Conference on Robotics and Automation*. IEEE Computer Society, 1989, pp. 431–432. [1](#)
- [11] D. Stewart, “A platform with six degrees of freedom,” *Proceedings of the institution of mechanical engineers*, vol. 180, no. 1, pp. 371–386, 1965. [1](#)

- [12] R. Clavel, "A Fast Robot with Parallel Geometry," in *Proc. Int. Symposium on Industrial Robots*, 1988, pp. 91–100. 1
- [13] B. Siciliano, "The Tricept Robot: Inverse Kinematics, Manipulability Analysis and Closed-Loop Direct Kinematics Algorithm," *Robotica*, vol. 17, no. 4, pp. 437–445, 1999. 1
- [14] C. Laschi *et al.*, "Soft robot arm inspired by the octopus," *Advanced Robotics*, vol. 26, no. 7, pp. 709–727, 2012. 1
- [15] D. Trivedi, C. D. Rahn, M. Kier, and I. D. Walker, "Soft Robotics : Biological Inspiration , State Of The Art , And Future Research," vol. 5, no. 3, pp. 99–117, 2008. 1
- [16] Rus, Daniela; Tolley, Michael T., "Design, Fabrication And Control Of Soft Robots," *Nature*, pp. 467–475, 2015. 1
- [17] D. Zambrano, M. Cianchetti, C. Laschi, H. Hauser, R. Füchslin, and R. Pfeifer, "The Morphological Computation Principles As A New Paradigm For Robotic Design," *Opinions and Outlooks on Morphological Computation*, pp. 214–225, 2014. 1
- [18] F. Renda, M. Giorelli, M. Calisti, M. Cianchetti, and C. Laschi, "Dynamic model of a multibending soft robot arm driven by cables," *IEEE Transactions on Robotics*, vol. 30, no. 5, pp. 1109–1122, 2014. 1
- [19] C. Messer, A. T. Mathew, N. Mladenovic, and F. Renda, "Ctr dapp: A python application for design and path planning of variable-strain concentric tube robots," in *2022 IEEE 5th International Conference on Soft Robotics (RoboSoft)*. IEEE, 2022, pp. 14–20. 1
- [20] J. M. Bern, K.-H. Chang, and S. Coros, "Interactive design of animated plushies," *ACM Transactions on Graphics (TOG)*, vol. 36, no. 4, p. 80, 2017. 2
- [21] J. M. Bern, G. Kumagai, and S. Coros, "Fabrication, modeling, and control of plush robots," in *2017 IEEE/RSJ International Conference on Intelligent Robots and Systems (IROS)*. IEEE, 2017, pp. 3739–3746. 2
- [22] T. Liu, S. Bouaziz, and L. Kavan, "Quasi-newton methods for real-time simulation of hyperelastic materials," *ACM Transactions on Graphics (TOG)*, vol. 36, no. 3, p. 23, 2017. 2
- [23] S. Bouaziz, S. Martin, T. Liu, L. Kavan, and M. Pauly, "Projective dynamics: fusing constraint projections for fast simulation," *ACM Transactions on Graphics (TOG)*, vol. 33, no. 4, p. 154, 2014. 2
- [24] O. Ogunmolu, X. Liu, N. Gans, and R. Wiersma, "Mechanism and Constitutive Model of a Continuum Robot for Head and Neck Cancer Radiotherapy," in *IEEE International Conference on Robotics and Automation (ICRA), Paris, France*, 2020. 2, 5, 9, 10
- [25] O. P. Ogunmolu, "A Multi-DOF Soft Robot Mechanism for Patient Motion Correction and Beam Orientation Selection in Cancer Radiation Therapy." Ph.D. dissertation, The University of Texas at Dallas; UT Southwestern Medical Center, 2019. 2, 3
- [26] F. Sterzing, R. Engenhart-Cabillic, M. Flentje, and J. Debus, "Image-guided radiotherapy: a new dimension in radiation oncology," *Deutsches Aerzteblatt International*, vol. 108, no. 16, p. 274, 2011. 2
- [27] J. Pikul, I. Cohen, and R. Shepherd, "Stretchable surfaces with programmable texture," May 2 2019, uS Patent App. 16/161,029. 2, 7
- [28] P. J. Keall, G. S. Mageras, J. M. Balter, R. S. Emery, K. M. Forster, S. B. Jiang, J. M. Kapatoes, D. A. Low, M. J. Murphy, B. R. Murray, *et al.*, "The Management of Respiratory Motion in Radiation Oncology Report of AAPM Task Group 76 A," *Medical physics*, vol. 33, no. 10, pp. 3874–3900, 2006. 2
- [29] A. Firouzeh, T. Higashisaka, K. Nagato, K. Cho, and J. Paik, "Stretchable kirigami components for composite meso-scale robots," *IEEE Robotics and Automation Letters*, vol. 5, no. 2, pp. 1883–1890, 2020. 3, 14
- [30] R. L. Truby, C. Della Santina, and D. Rus, "Distributed proprioception of 3d configuration in soft, sensorized robots via deep learning," *IEEE Robotics and Automation Letters*, 2020. 3, 14
- [31] A. Sedal, A. H. Memar, T. Liu, Y. Menguc, and N. Corson, "Design of deployable soft robots through plastic deformation of kirigami structures," *IEEE Robotics and Automation Letters*, 2020. 3, 14
- [32] A. Melnikov, L. Dorfmann, and R. W. Ogden, "Bifurcation of finitely deformed thick-walled electroelastic spherical shells subject to a radial electric field," *International Journal of Non-Linear Mechanics*, vol. 121, p. 103429, 2020. 3, 14
- [33] J. F. Canny and K. Y. Goldberg, "risc" industrial robotics: recent results and open problems," in *Proceedings of the 1994 IEEE international conference on robotics and automation*. IEEE, 1994, pp. 1951–1958. 3, 14
- [34] M. A. Erdmann and M. T. Mason, "An exploration of sensorless manipulation," *IEEE Journal on Robotics and Automation*, vol. 4, no. 4, pp. 369–379, 1988. 3, 14
- [35] M. T. Mason, *Mechanics of robotic manipulation*. MIT press, 2001. 3, 14
- [36] A. Belcher, "Patient Motion Management with 6-DOF Robotics for Frameless and Maskless Stereotactic Radiosurgery," Ph.D. dissertation, The University of Chicago, 2017. 3, 14
- [37] X. Liu, A. H. Belcher, Z. Grelewicz, and R. D. Wiersma, "Robotic stage for head motion correction in stereotactic radiosurgery," in *2015 American Control Conference (ACC)*. IEEE, 2015, pp. 5776–5781. 3, 14
- [38] X. Liu and R. D. Wiersma, "Optimization based trajectory planning for real-time 6DoF robotic patient motion compensation systems," *PloS one*, vol. 14, no. 1, p. e0210385, 2019. 1, 3, 14
- [39] D. G. McNeil, "M.R.I.'s Strong Magnets Cited in Accidents," *The New York Times*, pp. A–1, Aug 2005. [Online]. Available: <https://www.nytimes.com/2005/08/19/health/mris-strong-magnets-cited-in-accidents.html> 3, 14
- [40] B. Raaymakers, J. Lagendijk, J. Overweg, J. Kok, A. Raaijmakers, E. Kerkhof, R. Van der Put, I. Meijzing, S. Crijns, F. Benedosso, *et al.*, "Integrating a 1.5 t mri scanner with a 6 mv accelerator: proof of concept," *Physics in Medicine & Biology*, vol. 54, no. 12, p. N229, 2009. 3, 13, 14
- [41] J. J. Lagendijk, B. W. Raaymakers, A. J. Raaijmakers, J. Overweg, K. J. Brown, E. M. Kerkhof, R. W. van der Put, B. Hårdemark, M. van Vulpen, and U. A. van der Heide, "Mri/linac integration," *Radiotherapy and Oncology*, vol. 86, no. 1, pp. 25–29, 2008. 3, 13, 14
- [42] A. Méndez Romero, W. Wunderink, S. M. Hussain, J. A. De Pooter, B. J. Heijmen, P. C. Nowak, J. J. Nuyttens, R. P. Brandwijk, C. Verhoeft, J. N. Ijzermans, *et al.*, "Stereotactic body radiation therapy for primary and metastatic liver tumors: a single institution phase i-ii study," *Acta oncologica*, vol. 45, no. 7, pp. 831–837, 2006. 3, 13, 14
- [43] B. Raaymakers, I. Jürgenliemk-Schulz, G. Bol, M. Glitzner, A. Kotte, B. Van Asselen, J. De Boer, J. Bluemink, S. Hackett, M. Moerland, *et al.*, "First patients treated with a 1.5 t mri-linac: clinical proof of concept of a high-precision, high-field mri guided radiotherapy treatment," *Physics in Medicine & Biology*, vol. 62, no. 23, p. L41, 2017. 3, 14
- [44] R. Ogden, *Non-linear Elastic Deformations*. Mineola, New York: Dover Publications Inc., 1997. 3, 5, 7, 9
- [45] E. W. Weisstein. Spherical Coordinates. Accessed October 21, 2020. [Online]. Available: <https://mathworld.wolfram.com/SphericalCoordinates.html> 3
- [46] R. S. Rivlin and D. W. Saunders, "Large Elastic Deformations of Isotropic Materials. VII. Experiments on the Deformation of Rubber," *Philosophical Transactions of the Royal Society A: Mathematical, Physical and Engineering Sciences*, vol. 243, no. 865, pp. 251–288, 1950. 4
- [47] M. Mooney, "A theory of large elastic deformation," *Journal of applied physics*, vol. 11, no. 9, pp. 582–592, 1940. 4
- [48] C. Truesdell and W. Noll, *The Non-Linear Field Theories of Mechanics*. Springer, 1965. 5, 9
- [49] G. A. Holzapfel, T. C. Gasser, and R. W. Ogden, "A new constitutive framework for arterial wall mechanics and a comparative study of material models," *Journal of elasticity and the physical science of solids*, vol. 61, no. 1-3, pp. 1–48, 2000. 5
- [50] Y. Fung, P. Tong, and X. Chen, *Classical and computational solid mechanics*. World Scientific Publishing Company, 2001, vol. 2. 5
- [51] V.-D. Nguyen, "Constructing force-closure grasps," *The International Journal of Robotics Research*, vol. 7, no. 3, pp. 3–16, 1988. 7
- [52] D. J. Montana, "The Kinematics of Contact And Grasp," *The International Journal of Robotics Research*, vol. 7, no. 3, pp. 17–32, 1988. 7, 9
- [53] M. Spivak, "A Comprehensive Introduction to Differential Geometry. Vol. V. Berkeley: Publish or Perish," Inc. XI, 1979. 8
- [54] R. M. Murray and S. Sastry, "Grasping and Manipulation using Multi-fingered Robot Hands." in *Proceedings of Symposia in Applied Mathematics*, vol. 41, 1990, pp. 329–335. 8
- [55] J. R. Kerr, "An Analysis of Multi-Fingered Hands," *International Journal of Robotics Research*, no. Dept. of Mechanical Engineering, pp. 3–17, 1984. 10
- [56] J. J. Allen, L. M. Mäthger, A. Barbosa, and R. T. Hanlon, "Cuttlefish use visual cues to control three-dimensional skin papillae for camouflage," *Journal of Comparative Physiology A*, vol. 195, no. 6, pp. 547–555, 2009. 13
- [57] J. H. Pikul, S. Li, H. Bai, R. T. Hanlon, I. Cohen, and R. F. Shepherd, "Stretchable surfaces with programmable 3d texture morphing for synthetic camouflaging skins," *Science*, vol. 358, no. 6360, pp. 210–214, 2017. [Online]. Available: <https://science.sciencemag.org/content/358/6360/210> 13

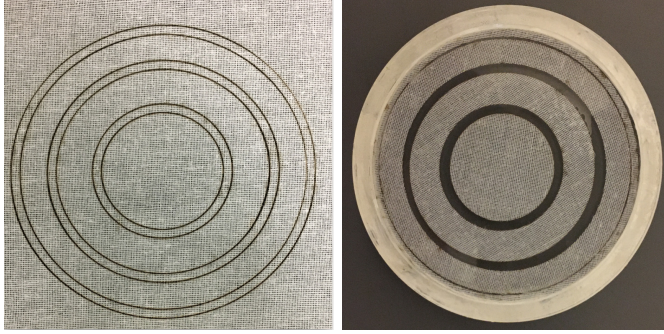


Fig. 11: (L) Concentric circular patterns. (R) Fabric in uncured silicone.

[58] S.-S. Yun, B. B. Kang, and K.-J. Cho, ‘‘Exo-glove pm: An easily customizable modularized pneumatic assistive glove,’’ *IEEE Robotics and Automation Letters*, vol. 2, no. 3, pp. 1725–1732, 2017. [13](#)

APPENDIX A ACTUATOR DESCRIPTION

This appendix is meant as a guide to designers to realize the mechanical feasibility of the proposed kinematic pairs that constitute the mechanism.

We fabricate Circumferential Constrained And Radially Symmetric Elastomeric (CCOARSE) Fiber Reinforced Elastomeric Enclosures (FREE), henceforth called Inflatable Air Bladders (IABs). Inspired by the behavior of the skin papillae of certain cephalopods (bivalves, mollusks, octopus and cuttlefish) that change their smooth, planar physical texture into 3D textures up to a specific maximum size [56] in less than 3 seconds [57], we pattern our IABs similar to the skin papillae of these organisms where the elasticity of the skin papillae is controlled by a muscular hydrostatic mechanism: an elastomeric dermis antagonizes the muscle’s fibers – causing uniaxial shape erection.

A. CCOARSE-FREE IAB Design

The soft actuator fabrication methodology is illustrated in Fig. 11. We used 3-D printed molds to make an elastomeric membrane of width 3 – 4 mm and radius $\approx 50\text{mm}$. To bear large deformations, we made the elastomeric membranes with Dragon Skin 10 (Smooth-On, Inc.), which have elongated properties of up to 1000% [58]. Given the low durometer hardness of Dragon Skin 10, Smooth-on Inc.(DS-10), it becomes fragile under high air pressure. We thus reinforce the elastomer with thin-layered fabric (Fleishman Fabrics & Supplies, Philadelphia, PA). The fabric is anisotropic: exhibiting high extensibility in the axial direction and low extensibility in the radial direction on a spherical-polar plane, for example. This fabric inhibits over-expansion of the elastomer and concentrates force along the axial direction, as a result.

The fabrication process proceeds as follows: (1) A thin-layered fabric (Fleishman Fabrics & Supplies, Philadelphia, PA) is first laser cut into circular patterns; (2) The cut meshes are removed and laid onto uncured silicone (DS-10) which has been poured into the 3-D printed mold; (3) We then add a silicone topcoat layer to the fabric-elastomer matrix before we allow it to cure at room temperature. (4) For rubber materials, sealing is not leak-proof as it is with metal parts. Therefore,

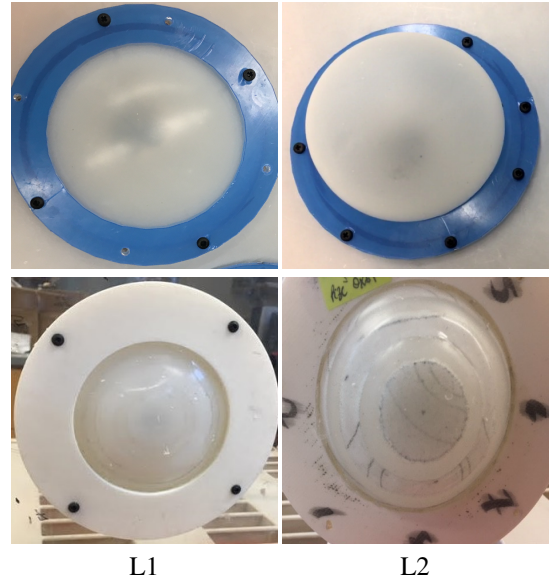


Fig. 12: Deformation of Elastomer-only (top) and Elastomeric-Fabric Matrix (bottom) under Low Air Pressurization (3-15psi).

we seal the fiber-reinforced rubber material by clamping it between 3D-printed polylactic acid (PLA) holders similar to an O-ring to make the enclosure airtight. As seen in Fig. 2, the circumference of the base part of the actuator locks into the PLA clamp at the bottom and by pressing the base from above and below, and fixing it with interspersed bolts at four points, the FREE is properly sealed while connected. (5) Compressed air can be passed through the pipe fitting connection into the enclosure as shown in the figure. (6) Nylon Phillips screws are used to further tighten the grip of the top clamp, the elastomeric-fiber matrix, and the bottom clamp so as to ensure that the enclosure is airtight.

The modules that comprise an actuator are connected to one another directly or through a spacer that connects rigid connecting elements. This fabrication method ensures that they can be easily adjoined, assembled or disassembled. As a result, the actuator is a little firm and well-fixated around a patient’s cranial region. As our IABs are customized to create pathways for assembly tools to access the bolt heads, we have been able to develop an assembly that minimizes volume.

The unique deformation pattern of the actuator is illustrated in Fig. 3. This deformation is similar to the way a balloon would stretch along its axial direction if a rope were tied around its circumference. Our proposed fabrication method allows users to rapidly iterate different designs with compressed low air pressure (at 3-15 psi), and it is advantageous because air is (i) cheaply available, (ii) environmentally-friendly, (iii) avoids electrical wirings, (iv) lightweight, and (v) inviscid. This aids a clean and safe human-robot workspace suitable for medical robotics applications such as in emerging magnetic resonance imaging-linear accelerators (MRI-Linacs) [40]–[42].

The experiments of Fig. 12 illustrate the deformation of the IAB with two different designs. The behavior at zero and full pressurization are indicated in each column. The top row shows the cured silicone without fabric while the bottom row

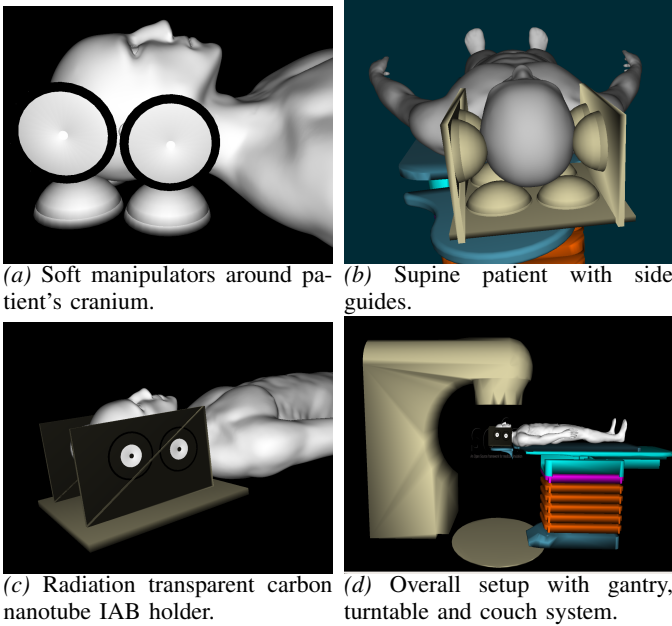


Fig. 13: System setup.

shows the cured elastomer with the entrenched fiber matrix. As seen, the fiber-free material exhibits a circumferential strain as well as radial strain while the fiber-constrained elastomer only exhibits a radial strain. As a result, we can generate a full *Gaussian deformation* and return to the reference planar configuration in 2-3 seconds, similar to the spikes produced by the skin papillae of the Octopus. These quick Gaussian spikes are useful for rapid manipulation, and push, and release of the head when the actuators are interconnected as linkages to fit a kinematician's desired mechanisms. For example, the soft compliance and tensile strength of this silicone material make it well-suited for treatment procedures where non-magnetic and radiation-transparent components can boost stereotactic precision as well as improve tumor control in MRI-LINACs.

B. Mechanism Setup

Explorative robotic positioning research studies have demonstrated the feasibility of maintaining stable patient cranial motion consistent with treatment plans using rigid Stewart-Gough platforms [36]–[38]. These achieve a $\leq 0.5\text{mm}$ and $\leq 0.5^\circ$ positioning accuracy 90% of the time. While aiding better clinical accuracy, they utilize rigid metallic components, electric motors and linear actuators which are not suitable for MRI imaging: they interfere with the magnets of the MRI machine, and can lead to patient fatality or significant damage to the MRI machine [39]. Time-resolved MRI techniques, which provide superior soft tissues image scans, can provide soft tissues delineation for use in brain or head and neck (H&N) radiation therapy (RT) [40]–[43]. Existing frame-based and frameless and maskless robotic motion correction mechanisms are not suitable for this because of their electro-mechanical parts that introduce radiation-attenuation and magnetic compliance concerns.

We position IABs around the patient's cranium as illustrated in Fig. 13. The IABs are held in place around the head by

a low-temperature rigid PVC foam insulation sheet, encased in carbon fiber to prevent radiation beam attenuation. Velcro stickers (not shown) hold the IABs in place. The freedoms provided by each IAB within the setup in Fig. 13b are described as follows: the side actuators correct head motion along the *left-right* axis of the head anatomy, including the yaw and roll motions, while the base IABs correct the head motion along the *anterior-posterior* axis [1, Ch. 2]. This arrangement offers prehensile manipulation via sensor-based motion manipulation strategies with flexible and electroelastic proprioceptive sensor plans [29]–[32]. By this, we mean the mechanical interactions of pushing or releasing by the IABs may be harnessed to further improve head manipulation robustness [33]–[35].

APPENDIX B DEFORMATION GRADIENT DERIVATION

It can be verified that the orthonormal basis vectors for (3) are

$$\mathbf{e}_r = \frac{\partial \mathbf{r}}{\partial r} / \left| \frac{\partial \mathbf{r}}{\partial r} \right| = \begin{bmatrix} \sin \phi \\ \cos \phi \end{bmatrix} \quad \mathbf{e}_\phi = \begin{bmatrix} \cos \phi \\ -\sin \phi \end{bmatrix}. \quad (75)$$

From (6), we can write

$$\begin{aligned} \mathbf{F} &= \frac{\partial(\mathbf{dx}_r)}{\partial R} \mathbf{e}_r \otimes \mathbf{e}_R + \frac{1}{R} \frac{\partial}{\partial \Phi} (\mathbf{dx}_r \mathbf{e}_r) \otimes \mathbf{e}_\Phi \\ &\quad + \frac{\partial}{\partial R} (\mathbf{dx}_\phi \mathbf{e}_\phi) \otimes \mathbf{e}_R + \frac{1}{R} \frac{\partial}{\partial \Phi} (\mathbf{dx}_\phi \mathbf{e}_\phi) \otimes \mathbf{e}_\Phi \end{aligned} \quad (76)$$

$$\begin{aligned} \mathbf{F} &= \frac{\partial(\mathbf{dx}_r)}{\partial R} \mathbf{e}_r \otimes \mathbf{e}_R + \frac{\mathbf{dx}_r}{R} \mathbf{e}_\phi \otimes \mathbf{e}_\Phi + \frac{1}{R} \frac{\partial(\mathbf{dx}_r)}{\partial \Phi} \mathbf{e}_r \otimes \mathbf{e}_\Phi \\ &\quad + \frac{\partial(\mathbf{dx}_\phi)}{\partial R} \mathbf{e}_\phi \otimes \mathbf{e}_R - \frac{\mathbf{dx}_\phi}{R} \mathbf{e}_r \otimes \mathbf{e}_\Phi + \frac{1}{R} \frac{\partial(\mathbf{dx}_\phi)}{\partial \Phi} \mathbf{e}_\phi \otimes \mathbf{e}_\Phi \end{aligned} \quad (77)$$

where we have made use of the chain rule, (4), together with the identities,

$$\frac{\partial \mathbf{e}_r}{\partial r} = \frac{\partial \mathbf{e}_\phi}{\partial r} = 0, \quad \frac{\partial \mathbf{e}_\phi}{\partial \phi} = -\mathbf{e}_r, \quad \frac{\partial \mathbf{e}_r}{\partial \phi} = \mathbf{e}_\phi. \quad (78)$$

in carrying out the partial derivatives of (77). In matrix form, we rewrite (77) as

$$\mathbf{F} = \begin{pmatrix} \frac{\partial(\mathbf{dx}_r)}{\partial R} & \frac{\partial(\mathbf{dx}_r)}{\partial \Phi} \\ \frac{\partial(\mathbf{dx}_\phi)}{\partial R} & \frac{\mathbf{dx}_r}{R} + \frac{1}{R} \frac{\partial(\mathbf{dx}_\phi)}{\partial \Phi} \end{pmatrix} \quad (79)$$

which from (4), becomes

$$\mathbf{F} = \begin{pmatrix} \frac{\partial(\mathbf{dx}_r)}{\partial R} & \frac{\partial(\mathbf{dx}_r)}{\partial \Phi} - \frac{\mathbf{dx}_\phi}{R} \\ \frac{\partial(\mathbf{dx}_\phi)}{\partial R} & \frac{\mathbf{dx}_r}{R} + \frac{1}{R} \frac{\partial(\mathbf{dx}_\phi)}{\partial \Phi} \end{pmatrix} = \begin{pmatrix} \frac{R^2}{r^2} & 0 \\ 0 & \frac{r}{R} + \frac{1}{R} \end{pmatrix}. \quad (80)$$

APPENDIX C ROBOT-HEAD DYNAMICS

We now derive the overall dynamics for the elastic IAB in Eulerian form. A point on the surface of the IAB has the following description

$$\mathbf{r} = \lambda \quad (81)$$

so that the Eulerian time differentiation of \mathbf{r} yields

$$\dot{\mathbf{r}} = \dot{\lambda} \quad (82)$$

Similarly, we find that $\ddot{\mathbf{r}}$ is

$$\ddot{\mathbf{r}} = \ddot{\lambda} \quad (83)$$

Recall the kinetic energy form of a continuum body (§ V)

$$T = \frac{1}{2} \rho \mathbf{v}(\mathbf{r}, t) \cdot \mathbf{v}(\mathbf{r}, t) = \frac{1}{2} \rho \dot{\mathbf{r}}^2. \quad (84)$$

A. Case I: Cauchy Elastic IAB Material Skins

Suppose we choose a Cauchy Elastic material so that the constitutive equation that governs the Cauchy stress tensor, σ , is independent of the path of the deformation from the reference configuration but is solely a function of the state of deformation. Then, it follows that $V = 0$. We have

$$T = \frac{1}{2} \rho \dot{\mathbf{r}}^2, \quad V = 0. \quad (85)$$

It follows that the Lagrangian is

$$L(\mathbf{r}, \dot{\mathbf{r}}) = \frac{1}{2} \rho \dot{\mathbf{r}}^2 \quad (86)$$

and the derivatives of the canonical momenta are

$$\frac{d}{dt} \frac{\partial L}{\partial \dot{\mathbf{r}}} = \frac{d}{dt} (\rho \dot{\mathbf{r}}) = \rho \ddot{\mathbf{r}}. \quad (87)$$

We have the following associated generalized forces

$$\frac{\partial L}{\partial r} = 0. \quad (88a)$$

Recalling the Euler-Lagrange equation from (48), we may write the torque that governs the j 'th IAB as (we have dropped the j 'th index)

$$\tau = \rho \ddot{r}. \quad (89)$$

B. Case II: Green Elastic IAB Material Skins

When the stress tensor depends on the strain, we have from (59), that

$$V(\mathbf{r}) = \text{tr}(\sigma \Sigma). \quad (90)$$

The associated force on the head is now a function of the kinetic and potential energies so that we have

$$L(\mathbf{r}, \dot{\mathbf{r}}) = \frac{1}{2} \rho \dot{\mathbf{r}}^2 + \text{tr}(\sigma \dot{\mathbf{F}}) \quad (91a)$$

$$= \frac{1}{2} \rho \dot{r}^2 + \text{tr}(\sigma \dot{\mathbf{F}}). \quad (91b)$$

Solving for the derivatives of the kinetic and potential energies as before, we have

$$\frac{d}{dt} \frac{\partial L}{\partial \dot{r}} = \rho \ddot{r} \quad (92a)$$

with the following associated generalized forces